Remote sensing of ocean color and aerosol properties: resolving the issue of aerosol absorption

Howard R. Gordon, Tao Du, and Tianming Zhang

Current atmospheric correction and aerosol retrieval algorithms for ocean color sensors use measurements of the top-of-the-atmosphere reflectance in the near infrared, where the contribution from the ocean is known for case 1 waters, to assess the aerosol optical properties. Such measurements are incapable of distinguishing between weakly and strongly absorbing aerosols, and the atmospheric correction and aerosol retrieval algorithms fail if the incorrect absorption properties of the aerosol are assumed. We present an algorithm that appears promising for the retrieval of in-water biophysical properties and aerosol optical properties in atmospheres containing both weakly and strongly absorbing aerosols. By using the entire spectrum available to most ocean color instruments (412–865 nm), we simultaneously recover the ocean's bio-optical properties and a set of aerosol models that best describes the aerosol optical properties. The algorithm is applied to simulated situations that are likely to occur off the U.S. East Coast in summer when the aerosols could be of the locally generated weakly absorbing Maritime type or of the pollution-generated strongly absorbing urban-type transported over the ocean by the winds. The simulations show that the algorithm behaves well in an atmosphere with either weakly or strongly absorbing aerosol. The algorithm successfully identifies absorbing aerosols and provides close values for the aerosol optical thickness. It also provides excellent retrievals of the ocean bio-optical properties. The algorithm uses a bio-optical model of case 1 waters and a set of aerosol models for its operation. The relevant parameters of both the ocean and atmosphere are systematically varied to find the best (in a rms sense) fit to the measured top-of-the-atmosphere spectral reflectance. Examples are provided that show the algorithm's performance in the presence of errors, e.g., error in the contribution from whitecaps and error in radiometric calibration. © 1997 Optical Society of America

1. Introduction

The Coastal Zone Color Scanner (CZCS) demonstrated the feasibility of measuring marine phytoplankton concentrations from Earth-orbiting sensors.[1,2] Based on the success of the CZCS, several similar instruments with a higher radiometric sensitivity and a larger number of spectral bands, e.g., the sea-viewing wide field-of-view sensor (SeaWIFS),[3] the moderate-resolution imaging spectroradiometer (MODIS),[4] will be launched in the near future. These ocean color instruments will actually measure the chlorophyll a concentration in the water as a surrogate for the phytoplankton concentration. In fact, the CZCS measured the sum of the concentrations of chlorophyll a and its degradation product phaeophytin a. This sum

was referred to as the pigment concentration C. Phytoplankton pigments have a broad absorption maximum in the blue ($\sim$435 nm) and a broad absorption minimum in the green ($\sim$565 nm), and the CZCS derived C from the ratio of the radiances backscattered out of the water (the water-leaving radiance L_w) near these two wavelengths.[5,6] Typically, L_w is at most 10% of the total radiance L_t, exiting the top of the atmosphere (TOA) in the blue and <5% in the green. Therefore it is necessary to extract L_w from L_t to derive C. This process is called atmospheric correction.

The atmospheric correction algorithm developed for the CZCS[6–10] is not sufficiently accurate for the new generation of sensors with higher radiometric sensitivity. Atmospheric correction of these sensors requires incorporation of multiple-scattering effects. Gordon and Wang[11,12] developed such an algorithm for SeaWIFS and found that the multiple-scattering effects depended on the physical and chemical properties of the aerosol (size distribution and refractive index). Therefore incorporation of multiple scattering into atmospheric correction required the introduction of aerosol models in the algorithm.

The Gordon and Wang algorithm is simple to describe. The spectral variation in L_t in the near-infrared (NIR) spectral region, where $L_w \approx 0$ in case 1 waters, is used to provide information concerning the aerosol's optical properties, as L_t there is due principally to Rayleigh scattering, which is known, and to aerosol scattering. The Rayleigh-scattering component is then removed, and the spectral variation of the remainder is compared with that produced by a set of candidate aerosol models in order to determine which two models of the candidate set are most appropriate. These models are then used to estimate the multiple-scattering effects. Gordon[12] has shown that this algorithm can provide L_w with the desired accuracy as long as the aerosol is weakly absorbing (more accurately, the aerosol must be weakly absorbing, and it must follow the relationship between size distribution and refractive index that is implicitly implied in the choice of the candidate aerosol models). Unfortunately, strongly absorbing aerosols, e.g., aerosols from anthropogenic urban sources or mineral dust transported from desert areas to the ocean, can possess size distributions similar to the weakly absorbing aerosols typically present over the oceans. As the spectral variation of aerosol scattering depends mostly on the aerosol size distribution and only weakly on the index of refraction, the spectral variation of scattering in the NIR is not sufficient to distinguish between weakly and strongly absorbing aerosols. Furthermore, in the case of mineral dust an additional complication arises: the dust is colored, i.e., its absorption is a function of wavelength.[13,14] Even if it were possible to estimate the absorption characteristics of mineral dust aerosol in the NIR, one would still not know the extent of the absorption in the visible. This is a particularly serious problem, as regions contaminated by mineral dust are often highly productive and thus important from a biogeochemical point of view. In fact, dust deposition may actually provide nutrients that enable the phytoplankton to bloom.[15]

The difficulty in detecting the presence of strongly absorbing aerosols is that the effects of absorption become evident only in the multiple-scattering regime. In the single-scattering regime, the reflectance of the aerosol is proportional to the product of the single-scattering albedo (ω_0) and the aerosol optical thickness (τ_a); i.e., at small τ_a there is no way to distinguish nonabsorbing aerosols ($\omega_0 = 1$) with a given τ_a from absorbing aerosols ($\omega_0 < 1$) and a larger τ_a. Retrieval of information concerning aerosol absorption requires multiple scattering; however, this multiple scattering need not be aerosol multiple scattering—when a low concentration of aerosol exists in the presence of strong Rayleigh scattering, e.g., in the blue, multiple Rayleigh scattering can increase the length of photon paths through the aerosol and enhance the chance of absorption. Also, if distributed vertically in the atmospheric column, the absorbing aerosol can reduce the Rayleigh-scattering component, which is otherwise large in the blue. Thus the possibility of inferring aerosol absorption is

increased as one progresses from the NIR into the visible, but unfortunately L_w is not known there (that is why atmospheric correction is required in the first place). The inescapable conclusion is that the Sea-WIFS algorithm[11] must fail when the aerosol is strongly absorbing unless the candidate aerosol models are restricted to those with similarly strong absorption properties.[12]

In addition to atmospheric correction, there is compelling interest in studying the global distribution and transport of aerosols because of their role in climate forcing and biogeochemical cycles.[16,17] Furthermore, not only is the aerosol concentration required, it is also important to know their absorption properties to understand their climatic effects. There has been continuing interest in measuring aerosol concentration from Earth-orbiting sensors.[18–24] Over the oceans these sensors generally utilize spectral bands for which the ocean can be assumed to be black ($L_w = 0$) or at least to have constant reflectance. In complete analogy to the atmospheric correction problem above, estimation of aerosol absorption properties from space fails for these sensors. The one exception is the retrieval of spatial distributions of an index indicating the presence of strongly absorbing aerosols by using the Total Ozone Mapping Spectrometer measurements in the ultraviolet.[25]

In this paper we describe an alternative approach to the problem of estimating oceanic biophysical properties for case 1 waters, as well as the physical–chemical properties of the aerosol, using spaceborne ocean color sensors. The approach is similar in spirit to that developed by Morel and co-workers[26,27] for CZCS and that proposed by Land and Haigh[28] for deriving case 2 water properties by using SeaWIFS. It utilizes all the spectral bands of the sensor. This ensures sufficient multiple scattering (Rayleigh scattering in the blue) to enable identification of the aerosol absorption, even at low aerosol concentrations. In order to separate the effects of aerosols from radiance backscattered from beneath the sea surface (L_w), we used a case 1 ocean color model in which the reflectance is related to the phytoplankton pigment concentration and the scattering properties of the phytoplankton and their associated detrital material. As with the SeaWIFS algorithm, several candidate aerosol models are employed: nonabsorbing, weakly absorbing, and strongly absorbing. Through a systematic variation of the candidate aerosols, phytoplankton scattering, C, and τ_a, a best fit to simulated spectral L_t data is obtained. It is found that the algorithm can successfully discriminate between weakly and strongly absorbing aerosols and can provide estimates of C, τ_a, and ω_0 with an accuracy that is nearly independent of ω_0. For consistency with an earlier paper,[12] we specifically examine a situation that is likely to be encountered off the U.S. East Coast in summer, that is, polluted continental air transported by the winds to the Middle Atlantic Bight. However, this situation is used only as an example to demonstrate the approach. We believe the approach could be applied to oceanic regions sub-

jected to mineral dust as well as aerosols resulting from biomass burning, given appropriate models for such aerosols.

We begin with a discussion of the approach and the modeling of the various quantities required for implementation. Next, we test the efficacy of the algorithm with simulated SeaWIFS[3] data. Recall that SeaWIFS has eight spectral bands centered at 412, 443, 490, 510, 555, 670, 765, and 865 nm. Finally, we examine the degradation of the performance of the algorithm in the presence of an L_t measurement error.

2. Algorithm Approach and Implementation

Rather than radiance L, we will use reflectance ρ defined as $\pi L/F_0 \cos \theta_0$, where F_0 is the extraterrestrial solar irradiance and θ_0 is the solar zenith angle. Then, neglecting the influence of direct Sun glitter, the total upwelling reflectance exiting the top of the atmosphere $\rho_t(\lambda)$ consists of the following components[11,12]: the pure Rayleigh- (molecular) scattering contribution $\rho_r(\lambda)$, the pure aerosol-scattering contribution $\rho_a(\lambda)$, the contribution that is due to the interaction effect between air molecules and aerosols $\rho_{ra}(\lambda)$, the contribution from whitecaps $t(\lambda)\rho_{wc}(\lambda)$, and the desired water-leaving contribution $t(\lambda)\rho_w(\lambda)$, i.e.,

$$\rho_t(\lambda) = \rho_r(\lambda) + \rho_a(\lambda) + \rho_{ra}(\lambda) + t(\lambda)\rho_{wc}(\lambda) + t(\lambda)\rho_w(\lambda),$$

(1)

where $t(\lambda)$ is the diffuse transmittance of the atmosphere. From the satellite image, we have the spectrum of the upwelling reflectance $\rho_t(\lambda)$. As $\rho_r(\lambda)$ depends only on the surface atmospheric pressure,[9,29] given an estimate of $t(\lambda)\rho_{wc}(\lambda)$ from a wind-speed estimate, it is not difficult to remove the pure Rayleigh-scattering and whitecap contributions $\rho_r(\lambda) + t(\lambda)\rho_{wc}(\lambda)$ from the total reflectance $\rho_t(\lambda)$:

$$[\rho_t(\lambda) - \rho_r(\lambda) - t(\lambda)\rho_{wc}(\lambda)] = [\rho_a(\lambda) + \rho_{ra}(\lambda)] + [t(\lambda)\rho_w(\lambda)]. \quad (2)$$

The known reflectance spectrum of $[\rho_t(\lambda) - \rho_r(\lambda) - t(\lambda)\rho_{wc}(\lambda)]$ consists of two parts that are difficult to separate, the water-leaving reflectance term $[t(\lambda)\rho_w(\lambda)]$ and the aerosol contribution $[\rho_a(\lambda) + \rho_{ra}(\lambda)]$, which includes the interaction term between aerosols and air molecules. The goal of atmospheric correction is to retrieve the water-leaving reflectance $\rho_w(\lambda)$ from the known reflectance $[\rho_t(\lambda) - \rho_r(\lambda) - t(\lambda)\rho_{wc}(\lambda)]$. Because of the high spatial and temporal variability of the physical, chemical, and optical properties of aerosols, it is difficult to estimate the aerosol contribution $[\rho_a(\lambda) + \rho_{ra}(\lambda)]$ to the total upwelling reflectance.

The basic assumption of the proposed algorithm is that for each aerosol and pigment concentration there is a unique and distinctive spectrum characteristic of its upwelling reflectances $[\rho_a(\lambda) + \rho_{ra}(\lambda)]$ and $[t(\lambda)\rho_w(\lambda)]$. In a given Sun-viewing geometry, similar (or close) spectra to $[\rho_t(\lambda) - \rho_r(\lambda) - t(\lambda)\rho_{wc}(\lambda)]$ can be obtained only from the atmosphere–ocean system by a combination of aerosols with similar optical

properties to the actual aerosol and a pigment concentration similar to that actually present in the ocean. That is, when we estimate $[t(\lambda)\rho_w(\lambda)]$ and $[\rho_a(\lambda) + \rho_{ra}(\lambda)]$ separately and form $[\rho_a(\lambda) + \rho_{ra}(\lambda)]'$ and $[t(\lambda)\rho_w(\lambda)]'$, where here and henceforth the primes will refer to computed or trial estimates, the computed reflectance spectrum

$$[\rho_t(\lambda) - \rho_r(\lambda) - t(\lambda)\rho_{wc}(\lambda)]' = [\rho_a(\lambda) + \rho_{ra}(\lambda)]' + [t(\lambda)\rho_w(\lambda)]'$$

will fit the true reflectance spectrum $[\rho_t(\lambda) - \rho_r(\lambda) - t(\lambda)\rho_{wc}(\lambda)]$ in the visible and NIR only if the computed water-leaving reflectance $[t(\lambda)\rho_w(\lambda)]'$ and the computed aerosol contribution $[\rho_a(\lambda) + \rho_{ra}(\lambda)]'$ fit their true values individually. In order to implement this idea, we need to be able to obtain estimates of $[t(\lambda)\rho_w(\lambda)]'$ and $[\rho_a(\lambda) + \rho_{ra}(\lambda)]'$. We now describe how this is accomplished.

A. Water Component $t\rho_w$

The prediction of the water-leaving reflectance, $\rho_w(\lambda)$, is affected with the semiempirical bio-optical radiance model, developed by Gordon et al.[30] for case 1 waters,[5,31] i.e., waters for which the optical properties are controlled by the water itself and by the concentration of phytoplankton and their decay products. Since we use the pigment concentration C as a surrogate for the phytoplankton concentration, one would expect that the absorption and scattering properties of the particles would depend only on C; however, it is found for such waters that for a given C the total scattering coefficient varies by roughly a factor of 2.[5] Thus a second scattering-related parameter b^0, which ranges from 0.12 to 0.45 m^{-1} with a mean value of 0.30 m^{-1} (when C has units of milligrams per cubic meter), is introduced. Gordon et al.[30] found that by using such a model the water-leaving radiance dependence on C in case 1 waters could be explained. Similar results were also obtained by Bricaud and Morel.[26] This bio-optical ocean color model actually provides the normalized water-leaving reflectance,[6,12] $[\rho_w(\lambda)]_N$, defined by

$$[\rho_w(\lambda)]_N \equiv \rho_w \exp[+(\tau_r/2 + \tau_{Oz})/\cos \theta_0],$$

where τ_r and τ_{Oz} are the Rayleigh and ozone optical thicknesses of the atmosphere, respectively. Sample spectra of $[\rho_w(\lambda)]_N$ as a function of C and b^0 are shown in Fig. 1. Clearly, the normalized water-leaving reflectance is sensitive to the pigment concentration C for short wavelengths (412 and 443 nm) and small pigment concentration ($C \lesssim 0.4$ mg/m³). For longer wavelengths (555 and 670 nm) or large pigment concentrations ($C \gtrsim 0.8$ mg/m³), $[\rho_w(\lambda)]_N$ does not depend significantly on the pigment concentration C. It is taken to be zero at 765 and 865 nm.

It should be noted that the Gordon et al.[30] reflectance model above does not take into account the bidirectional effects of the subsurface upwelled spectral radiance; i.e., it assumes that the upwelling radiance beneath the sea surface is totally diffuse.
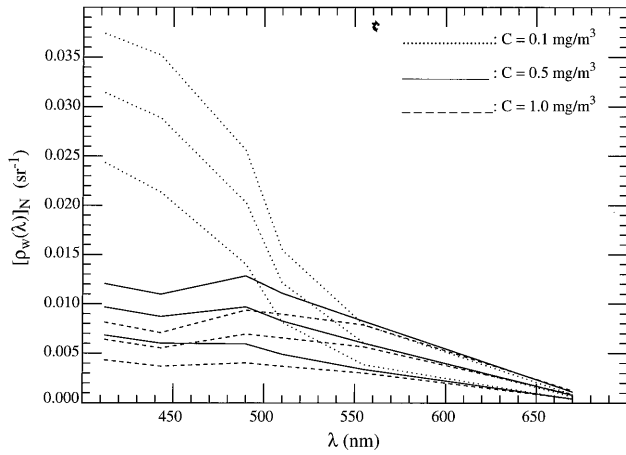
Fig. 1. Spectrum of normalized water-leaving reflectance $[\rho_w(\lambda)]_N$ for pigment concentrations of 0.1, 0.5, and 1.0 mg/m^3. For each pigment concentration, from the top to the bottom curves, the values of coefficient b^0 are 0.45, 0.30, and 0.12 m^{-1}, respectively.

Morel and co-workers[32–35] have demonstrated that this is not the case; however, as Morel and Gentili[35] have shown, bidirectional effects can be easily introduced into the model and described as a function of C (and, if necessary, b^0).

Once $\rho_w(\lambda)$ is determined, it is necessary to propagate it to the TOA. As mentioned earlier, this is accomplished with the diffuse transmittance $t(\lambda)$. Tanre et al.[36] and Gordon et al.[6] provided simple expressions for $t(\lambda)$ that include the effects of both aerosol and Rayleigh scattering. Later, Yang and Gordon[37] provided a detailed analysis of $t(\lambda)$ based on precise computations. They showed that (1) bidirectional effects play a role in t only in the blue and only at low C, (2) aerosols have a significant effect on t only if they are strongly absorbing, (3) t is independent of the aerosol vertical structure even if the aerosol is strongly absorbing, and (4) given an aerosol model, it is simple to predict the correct value of t for any aerosol concentration and viewing geometry. The value of t can be precisely computed given C (to provide bidirectional effects), an aerosol model (to provide the aerosol properties), and the aerosol optical thickness $\tau_a(\lambda)$ (to provide the aerosol concentration). However, for the purposes of this paper, we will approximate t by assuming it is independent of the aerosol. In this case, $t(\lambda)$ is given by

$$t(\lambda) = \exp\{-[\tau_r(\lambda)/2 + \tau_{Oz}(\lambda)]/\cos\theta_v\}, \quad (3)$$

where θ_v is the angle between the zenith and a line from the sensor to the pixel under consideration. Thus the simulated $t(\lambda)\rho_w(\lambda)$ is given by

$$t(\lambda)\rho_w(\lambda) = [\rho_w(\lambda)]_N \exp\left\{-[\tau_r(\lambda)/2 + \tau_{Oz}(\lambda)]\right.$$
$$\left.\times \left(\frac{1}{\cos\theta_0} + \frac{1}{\cos\theta_v}\right)\right\}. \quad (4)$$

B. Aerosol Component $\rho_a + \rho_{ra}$

Gordon and Wang[11] have shown that the multiple-scattering effects in $\rho_a + \rho_{ra}$ depend significantly on the physical and chemical properties of the aerosol, i.e., their size distribution and their refractive index. Thus aerosol models have to be introduced to incorporate multiple-scattering effects in atmospheric correction. Similarly, aerosol models are also required to retrieve aerosol properties from space observations.[38,39] Gordon and Wang[11] used aerosol models that were developed by Shettle and Fenn[40] for LOWTRAN 6.[41] These models consist of particles distributed in size according to combinations of two log-normal distributions and are described in detail in Ref. 12. Briefly, four models at four different relative humidities are used here. These are the maritime (M), the coastal (C), the tropospheric (T), and the urban (U). The relative humidities (RH's) used are 50%, 70%, 90%, and 99%. We denote a particular model by a letter and a number, e.g., M99 refers to the maritime model at 99% RH. There is an increasing amount of absorption as one progresses through M, C, T, to U. For example, at 865 nm the aerosol single-scattering albedo ω_0 is 0.9934, 0.9884, and 0.9528, respectively, for the maritime, coastal, and
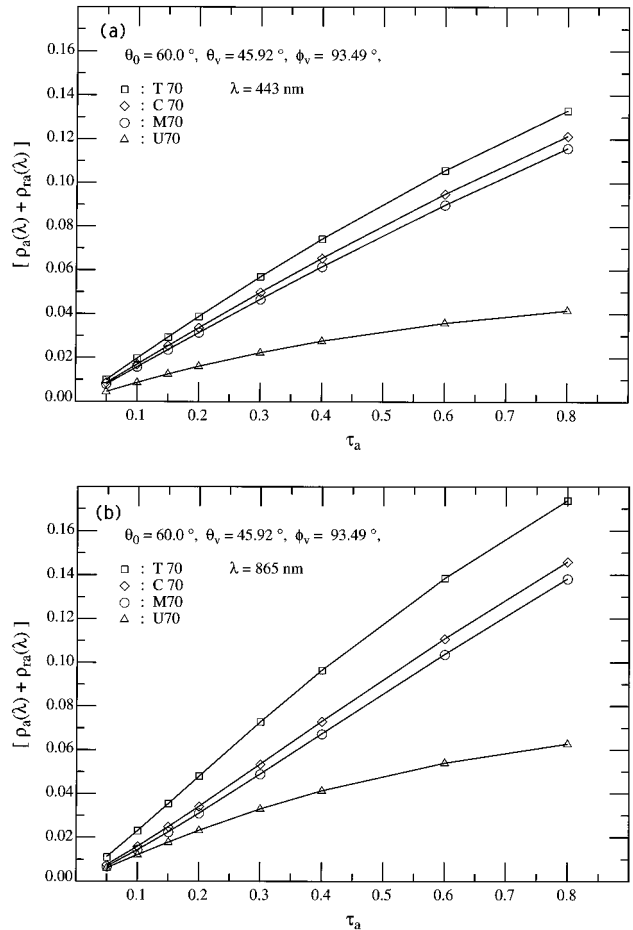

Fig. 2. Curve fits of $[\rho_a(\lambda) + \rho_{ra}(\lambda)]$ versus τ_a for aerosol models M70, C70, T70, and U70 with $\theta_0 = 60.0°$, $\theta_v = 45.92°$, and $\phi_v = 93.49°$: (a) 443 and (b) 865 nm.

Aerosols	Candidate Models at RH				Test Models at RH
	50%	70%	90%	99%	80%
M	0.9814	0.9859	0.9953	0.9986	0.9934
C	0.9705	0.9768	0.9919	0.9974	0.9884
T	0.9295	0.9346	0.9698	0.9870	0.9528
U	0.6026	0.6605	0.8206	0.9419	0.7481

tropospheric models (80% RH), whereas, in contrast, $\omega_0 = 0.7481$ for the urban model. Here the urban model is intended to represent the strongly absorbing aerosols that might be present over the oceans near areas with considerable urban pollution, e.g., the Middle Atlantic Bight off the U.S. East Coast in summer. Table 1 provides the absorption properties of the candidate aerosol models and the test aerosol models at 865 nm. Note the coarse resolution in ω_0 for the urban models compared with the others.

We employ these 16 aerosol models as candidates to test the algorithm. For a two-layer atmosphere, with the aerosol confined to the bottom layer, the scalar radiative transfer equation (polarization ignored) was solved for each of the 16 candidate aerosol models (M, C, T, and U aerosols with 50%, 70%, 90%, 99% RH) with eight values of $\tau_a(\lambda)$ in the range of 0.05–0.8 at each wavelength λ, for solar zenith angle $\theta_0 = 0$–80° in increments of 2.5°, and for 33 different viewing zenith angles with θ_v in the range of 0–90°. It is difficult to have this large computational set of

aerosol optical thickness are presented in Fig. 2 for a Sun-viewing geometry with $\theta_0 = 60°$, $\theta_v \approx 46°$, and $\phi_v \approx 93°$. This geometry has relatively large errors in the fits compared with the other geometries used here. It can be seen that the method of using Eq. (5) and Fourier expanding its coefficients is appropriate for computing $[\rho_a(\lambda) + \rho_{ra}(\lambda)]$ for any candidate aerosol model, at any Sun-viewing geometry, aerosol optical thickness, and wavelength. The largest fitting errors occurred at the largest wavelength ($\lambda = 865$ nm) and small aerosol optical thickness ($\tau_a \approx 0.1$). They were of the order of 1–2%.

C. Algorithm Implementation

We experimented with several approaches for implementing the algorithm. The one we found most effective is summarized as follows:

First, for the given Sun-viewing geometry (θ_0, θ_v, ϕ_v), we vary the value of aerosol optical thickness at 865 nm, $\tau_a(865)$, for each candidate aerosol model to provide the aerosol component $[\rho_a(\lambda) + \rho_{ra}(\lambda)]'$. We then vary the pigment concentration C and the scattering-related coefficient b^0 to provide the water-leaving reflectance $[t(\lambda)\rho_w(\lambda)]'$. These yield a trial upwelling reflectance $[\rho_t(\lambda) - \rho_r(\lambda) - t(\lambda)\rho_{wc}(\lambda)]'$ at each of N bands of the ocean color sensor.

Second, we compute the percent deviation δ' of this simulated spectrum $[\rho_t(\lambda) - \rho_r(\lambda) - t(\lambda)\rho_{wc}(\lambda)]'$ from the measured true spectrum $[\rho_t(\lambda) - \rho_r(\lambda) - t(\lambda)\rho_{wc}(\lambda)]$ over the N spectral bands for each test set $(A, \tau_a, C, b^0)'$, where A labels the candidate aerosol model. The percent deviation $\delta(A, \tau_a, C, b^0)'$ is de-

$$\delta(A, \tau_a, C, b^0)' = 100\% \left(\frac{1}{N-1} \sum_{i=1}^{N} \left\{ \frac{[\rho_t(\lambda_i) - \rho_r(\lambda_i) - t(\lambda_i)\rho_{wc}(\lambda_i)] - [\rho_t(\lambda_i) - \rho_r(\lambda_i) - t(\lambda_i)\rho_{wc}(\lambda_i)]'}{[\rho_t(\lambda_i) - \rho_r(\lambda_i) - t(\lambda_i)\rho_{wc}(\lambda_i)]} \right\}^2 \right)^{1/2}. \quad (6)$$

values of $[\rho_a(\lambda) + \rho_{ra}(\lambda)]$ available for image processing for all the aerosol candidates, aerosol optical thicknesses, Sun-viewing geometries (θ_0, θ_v, ϕ_v, where ϕ_v is the azimuth of the viewing direction relative to the Sun), and spectral bands; therefore, in a manner similar to the Gordon and Wang algorithm,[12] lookup tables (LUT) are used to provide $[\rho_a(\lambda) + \rho_{ra}(\lambda)]$. In the Gordon and Wang algorithm the LUT related $[\rho_a(\lambda) + \rho_{ra}(\lambda)]$ to $\rho_{as}(\lambda)$, the single-scattered aerosol reflectance. Equivalently, we relate the term $[\rho_a(\lambda) + \rho_{ra}(\lambda)]$ to the aerosol optical thickness τ_a; our simulated values of $[\rho_a(\lambda) + \rho_{ra}(\lambda)]$ are fit to

$$[\rho_a(\lambda) + \rho_{ra}(\lambda)] = a(\lambda)\tau_a + b(\lambda)\tau_a^2 + c(\lambda)\tau_a^3 + d(\lambda)\tau_a^4 \quad (5)$$

with least squares. To reduce storage further, coefficients $a(\lambda)$, $b(\lambda)$, $c(\lambda)$, and $d(\lambda)$ were expanded in Fourier series in the relative azimuth view angle ϕ_v, and only the Fourier coefficients were stored in the LUT. Samples of the fit of $[\rho_a(\lambda) + \rho_{ra}(\lambda)]$ to the

fined in the sense of rms:

Third, we sort the deviations $\delta(A, \tau_a, C, b^0)'$ to find the best ten sets of $(A, \tau_a, C, b^0)'$, which yield the ten smallest percent deviations $\delta(A, \tau_a, C, b^0)'$.

Fourth, as the correct aerosol model is unlikely to be identical to one of the candidates, we assume that the characteristics of aerosols and pigment concentration can be adequately described by these best ten sets of parameters $(A, \tau_a, C, b^0)'$. The retrieved single-scattering albedo ω_0' and optical thickness τ_a' of the aerosols and $b^{0'}$ and the pigment concentration C' in the ocean are then computed by averaging ω_0', τ_a', $b^{0'}$, and C' over the best ten sets of $(A, \tau_a, C, b^0)'$.

We considered applying standard multivariable minimization techniques[42] to find the smallest δ'; however, because of the discrete nature of the candidate models, this would have yielded at best the minimum δ' for each test model A. By using the algorithm described above, we found that unless the actual aerosol was close to one of the candidate mod-

Table 2. Mean Values of Retrieved $\omega_0{}'(865)$ for the Seven Sun-Viewing Geometries and Each of Four Aerosol Models[a]

Models	C (mg/m^3)	0.100	0.500	1.000
M80	$\tau_a(865) = 0.100$	0.992 (0.43%)	0.996 (0.14%)	0.997 (0.10%)
$\omega_0 = 0.993$	$\tau_a(865) = 0.200$	0.995 (0.10%)	0.995 (0.10%)	0.996 (0.05%)
	$\tau_a(865) = 0.300$	0.996 (0.05%)	0.996 (0.06%)	0.996 (0.10%)
C80	$\tau_a(865) = 0.100$	0.980 (0.97%)	0.972 (1.60%)	0.965 (2.26%)
$\omega_0 = 0.988$	$\tau_a(865) = 0.200$	0.983 (0.53%)	0.988 (0.31%)	0.989 (0.41%)
	$\tau_a(865) = 0.300$	0.987 (0.25%)	0.987 (0.27%)	0.987 (0.37%)
T80	$\tau_a(865) = 0.100$	0.952 (0.78%)	0.935 (0.13%)	0.935 (0.00%)
$\omega_0 = 0.953$	$\tau_a(865) = 0.200$	0.946 (0.34%)	0.936 (0.44%)	0.940 (1.41%)
	$\tau_a(865) = 0.300$	0.945 (0.31%)	0.934 (0.04%)	0.945 (1.82%)
U80	$\tau_a(865) = 0.100$	0.793 (4.21%)	0.761 (4.51%)	0.769 (3.36%)
$\omega_0 = 0.748$	$\tau_a(865) = 0.200$	0.730 (4.76%)	0.750 (8.25%)	0.712 (7.44%)
	$\tau_a(865) = 0.300$	0.730 (5.14%)	0.784 (2.56%)	0.699 (7.34%)

[a]The standard deviation divided by the mean is listed in parentheses.

els, the minimum of δ' was shallow, so the model yielding the minimum was not necessarily much better than other models with small changes in the parameters. Furthermore, we observed that it was rare that only one candidate model was chosen among the ten best, i.e., the nth best for one A might be superior to the best for another A. Were the candidate models dense, in the sense that the actual aerosol would always be close to one of the candidates, multivariable minimization techniques would have been used.

3. Algorithm's Performance

In this section we examine the performance of the algorithm by applying it to simulated SeaWIFS[3] data. The Sun-viewing geometries are taken as those used in Refs. 11 and 12: viewing at the center of the scan (viewing zenith angle $\theta_v \approx 1°$) for solar zenith angle $\theta_0 = 20°$, 40°, and 60° and viewing at the edge of the scan ($\theta_v \approx 45°$) near the perpendicular plane ($\phi_v = 90°$) for $\theta_0 = 0°$, 20°, 40°, and 60°. These cover much of the range of Sun-viewing geometries available to SeaWIFS. Pseudodata were provided by solving the scalar radiative transfer equation for a two-layer atmosphere system with a specified aerosol confined in the lower layer. The pseudo water-leaving reflectance $\rho_w(\lambda)$ was provided for $b^0 = 0.30$ m^{-1} (the mean value for case 1 waters)[5] and pigment concentrations $C = 0.1$, 0.5, and 1.0 mg/m^3.

The algorithm attempts to match the pseudodata spectrum of $\rho_t(\lambda) - \rho_r(\lambda) - t(\lambda)\rho_{wc}(\lambda)$ by varying the aerosol model among the 16 candidates ($N_A = 16$), the aerosol optical thickness $\tau_a(865)$ from 0.01 to 0.40 in increments of 0.01 ($N_\tau = 40$), the pigment concentration from 0.05 to 1.50 mg/m^3 in increments of 0.05 mg/m^3 ($N_C = 30$), and finally, b^0 from 0.12 to 0.45 m^{-1} in increments of 0.03 m^{-1} ($N_b = 12$). The total number of elements in the test set (A, τ_a, C, b^0)$'$ is $N = N_A \times N_\tau \times N_C \times N_b = 16 \times 40 \times 30 \times 12 = 230,400$.

For the first test of the algorithm, we examined cases in which the aerosol optical properties of the pseudoatmosphere were included in the candidate aerosol models, i.e., the aerosol optical properties in

the atmosphere system were taken from M70, C70, T70, and U70. The optical thickness at 865 nm was taken to be $\tau_a(865) = 0.1$, 0.2, or 0.3. The main purpose of this was to test the code for implementation of the algorithm. In all cases, for the best set (smallest δ'), the correct aerosol model and the correct values of the parameters were chosen. In fact, δ' for the correct set was a small fraction of a percent and $\sim$10–30 times smaller than the second best set. The residual error was due to small errors in the LUT caused by the least-squares and Fourier analysis. Even the averages over the best ten sets were excellent, providing close values of $\tau_a(865)$, b^0, and C. As the aerosol single-scattering albedo ω_0 is a weak function of wavelength λ, we use the retrieved value at 865 nm, $\omega_0(865)$ (averaged over the best ten sets), as an indication of the algorithm's ability to distinguish between weakly and strongly absorbing aerosols. The derived values of $\omega_0(865)$ showed that weakly and strongly absorbing aerosols are easily recognized by the algorithm.

As it is unlikely for the aerosols in the atmosphere to have exactly the same optical properties as any one of candidate aerosol models, we tested more realistic cases in which the aerosol models were similar to, but not the same as any of, the 16 candidate aerosol models. Following Gordon[12] the aerosol models M80, C80, T80, and U80 (Shettle and Fenn models with 80% RH) were chosen for this purpose (Table 1). We begin by describing the results obtained from averaging the parameters from the sets with the ten smallest values of δ'. The averaged $\omega_0{}'(865)$, $\tau_a{}'(865)$, and C' for a given geometry are taken to be the retrieved values of these parameters. To estimate the performance on a more global scale, i.e., for the full range of Sun-viewing geometries, we then average over all seven Sun-viewing geometries and compute the mean and the standard deviation in the retrieved parameter values. The mean values of retrieved aerosol single-scattering albedo $\omega_0{}'(865)$ are provided in Table 2 for a pseudoatmosphere characterized by the aerosol models M80, C80, T80, and U80. It can be seen from Table 2 that the retrieved results for ω_0 are good for each of the four pseudoaero-

Table 3. Mean Values of Retrieved C' for Seven Sun-Viewing Geometries and Four Aerosol Models[a]

C (mg/m^3)	0.100	0.500	1.000
$\tau_a(865) = 0.100$	0.100 (1.90%)	0.528 (7.30%)	1.098 (11.7%)
$\tau_a(865) = 0.200$	0.101 (4.56%)	0.547 (15.2%)	0.982 (23.9%)
$\tau_a(865) = 0.300$	0.101 (4.42%)	0.612 (24.1%)	0.947 (31.3%)

[a]The standard deviation divided by the mean is listed in parentheses.

Table 5. Percentage of Retrieved Pigment Concentration C' Within Certain Error Limits for Aerosol Models M80, C80, T80, and U80

C (mg/m^3)	$\Delta C/C$	<5%	<10%	<20%	<30%
0.1	$\tau_a(865) = 0.100$	96%	100%	100%	100%
	$\tau_a(865) = 0.200$	89%	92%	100%	100%
	$\tau_a(865) = 0.300$	89%	92%	100%	100%
0.5	$\tau_a(865) = 0.100$	32%	75%	92%	100%
	$\tau_a(865) = 0.200$	32%	50%	75%	89%
	$\tau_a(865) = 0.300$	25%	35%	64%	75%
1.0	$\tau_a(865) = 0.100$	21%	50%	71%	96%
	$\tau_a(865) = 0.200$	28%	39%	57%	71%
	$\tau_a(865) = 0.300$	14%	25%	50%	60%

sol models. Large percent deviations (the standard deviation over the seven geometries divided by the mean) in the range of 3% to ~8%, are encountered for the strongly absorbing U80 aerosol model, because of the coarse resolution in the value of ω_0 for the candidates (Table 1). Nevertheless, the algorithm can distinguish between the weakly absorbing aerosols (M80, C80, T80) and the strongly absorbing aerosol (U80) without difficulty.

Since the ultimate goal of ocean color remote sensing is to estimate the phytoplankton pigment concentration, we now examine the retrieval of C using the algorithm. Table 3 presents the mean values of retrieved C', which are averaged over seven Sun-viewing geometries and also over the four test aerosol models, M80, C80, T80, and U80 (28 cases in all). It can be observed that the retrieved results of pigment concentration are reasonable for all three tested aerosol optical thicknesses [$\tau_a(865) = 0.1, 0.2,$ and 0.3] and all three pigment concentrations [$C = 0.1, 0.5,$ and 1.0 mg/m^3]. For the small pigment concentration, $C = 0.1$ mg/m^3, or for small aerosol optical thickness, $\tau_a(865) = 0.1$, the spectrum-matching algorithm still works well. With an increase in either pigment concentration or aerosol concentration, the percent deviations and percent errors in the retrieved C' become larger. For comparison, Table 4 provides similar results, for the weakly absorbing aerosols only, by using the Gordon and Wang correction algorithm.[12] Note that the present algorithm behaves as well as the Gordon and Wang algorithm, even when strongly absorbing aerosols are included. Had strongly absorbing aerosols been included in Table 4, the results would have been significantly poorer, e.g., in many cases it would have been impossible even to compute C because one or both of the required $\rho_w(443)$ and $\rho_w(555)$ would be negative.

Detailed retrievals of the pigment concentration C are tabulated in Table 5, which gives the percentages

Table 4. Mean Values of Retrieved C' for Seven Sun-Viewing Geometries and Three Aerosol Models (M80, C80, T80) derived with the Gordon and Wang[11] Algorithm[a]

C (mg/m^3)	0.10	0.47	0.91
$\tau_a(865) = 0.100$	0.101 (1.6%)	0.466 (3.4%)	0.912 (9.1%)
$\tau_a(865) = 0.200$	0.100 (3.1%)	0.470 (4.7%)	0.940 (12.8%)
$\tau_a(865) = 0.300$	0.098 (5.5%)	0.493 (15.3%)	0.936 (25.3%)

[a]The standard deviation divided by the mean is listed in parentheses.

of cases with relative error in the retrieval, $|\Delta C|/C$, less than 5%, 10%, 20%, and 30%. For the smallest pigment concentration, in all the 84 cases examined (three aerosol optical thicknesses, four aerosol models, and seven Sun-viewing geometries), $|\Delta C|/C$ was always <20%, and even <5% for ~90% of the cases. For a pigment concentration of $C = 0.5$ mg/m^3 and for small aerosol optical thickness, $\tau_a(865) = 0.1$, all individual simulations have $|\Delta C|/C < 30\%$, while for $\tau_a(865) = 0.2$ there are ~89% of the cases with $|\Delta C|/C < 30\%$, and for $\tau_a(865) = 0.3$ there are ~75% of the cases with $|\Delta C|/C < 30\%$. At the highest pigment concentration examined (1.0 mg/m^3), for small aerosol optical thickness the algorithm still performs well with only three cases with $|\Delta C|/C > 30\%$. However, as $\tau_a(865)$ increases, the errors become larger, and ~71% of the cases have $|\Delta C|/C < 30\%$ for $\tau_a(865) = 0.2$ and only ~60% for $\tau_a(865) = 0.3$.

The algorithm clearly works better to estimate C for smaller pigment concentrations, which can be explained by the relationship between the (normalized) upwelling water-leaving reflectance and the pigment concentration (Fig. 1). As we showed in Section 2, the water-leaving reflectance depends strongly on pigment concentration C when C is small ($C \lesssim 0.4$ mg/m^3). At small C, a small change in C (0.05 mg/m^3 in the algorithm) will result in a significant change in the upwelling water-leaving reflectance. However, when pigment concentration is as large as ~1.0 mg/m^3, the upwelling water-leaving reflectance is only a weak function of pigment concentration, and a small change of 0.05 mg/m^3 in C does not result in a significant change in the upwelling water-leaving reflectance. This causes the larger percent deviation in C when the algorithm is applied to larger pigment concentrations.

Mean values of the retrieved aerosol optical thickness $\tau_a'(865)$ over the seven Sun-viewing geometries and four testing aerosol models (M80, C80, T80, and U80) are presented in Table 6. The mean values are close to their corresponding true aerosol optical thicknesses, the percent deviations range from ~6% to ~11%.

Figure 3 provides samples of the three best sets (A, τ_a, C, b^0) determined by the algorithm for aerosol models of M80, C80, T80, and U80 with $\tau_a(865) = 0.2$ and $C = 0.5$ mg/m^3, for a single Sun-viewing geom-

Table 6. Mean Values of Retrieved $\tau_a{}'(865)$ for Seven Sun-Viewing Geometries and Four Aerosol Models (M80, C80, T80, U80)[a]

C (mg/m³)	0.100	0.500	1.000
$\tau_a(865) = 0.100$	0.102 (8.94%)	0.101 (10.2%)	0.102 (11.6%)
$\tau_a(865) = 0.200$	0.201 (6.31%)	0.199 (8.53%)	0.199 (8.20%)
$\tau_a(865) = 0.300$	0.300 (6.22%)	0.294 (8.79%)	0.300 (9.93%)

[a]The standard deviation divided by the mean is listed in parentheses.

etry ($\theta_0 = 20°$, $\theta_v = 45.92°$, $\phi_v = 90°$). As the pseudoaerosol models (M80, C80, T80, and U80) are similar to the candidate models used in the algorithm (M, C, T, and U with 50%, 70%, 90%, and 99% RH) but are not identical to any of 16 candidates, there is no correct aerosol model for the algorithm to choose to match the upwelling reflectance $[\rho_a(\lambda) + \rho_{ra}(\lambda)] + [t(\lambda)\rho_w(\lambda)]$. Figure 3 shows that the aerosol models that have optical properties similar to those of the test aerosol models are selected first by the algorithm. Even though there are some errors caused by picking the incorrect aerosol models, the pigment concentration chosen by the algorithm is close to its

true value (0.5 mg/m³ in Fig. 3). For the four pseudoaerosol models tested, the percent deviations of the best match for whole spectrum $\delta(A, \tau_a, C, b^0)'$ varied from ~0.7% to 1.1%. Unlike the case when the test aerosol was one of the candidates, there was no significant increase in δ' from the best set to the second best set, etc. For the best ten sets, the largest percent deviation for $C = 0.5$ mg/m³ is ~1.5%.

Figure 3 also shows the reason for our basic assumption that a good fit is obtained only if the spectra of $t\rho_w'$ and $[\rho_a + \rho_{ra}]'$ individually fit $t\rho_w$ and $\rho_a + \rho_{ra}$: the spectral shapes of $\rho_a + \rho_{ra}$ (Fig. 3, lower curves) and $t\rho_w$ (Fig. 1) are usually quite different. This is particularly true for low values of C.

From these tests of the algorithm we conclude that it can detect the presence of strongly absorbing aerosols successfully. Whenever the optical properties of aerosol in the atmosphere are the same (or close) to that of any of the 16 candidate aerosol models employed in the algorithm, the retrieved pigment concentration C will be excellent, meeting the requirements of SeaWIFS and MODIS. If the optical properties of the aerosol in the atmosphere are similar to that of any candidate aerosol model, the
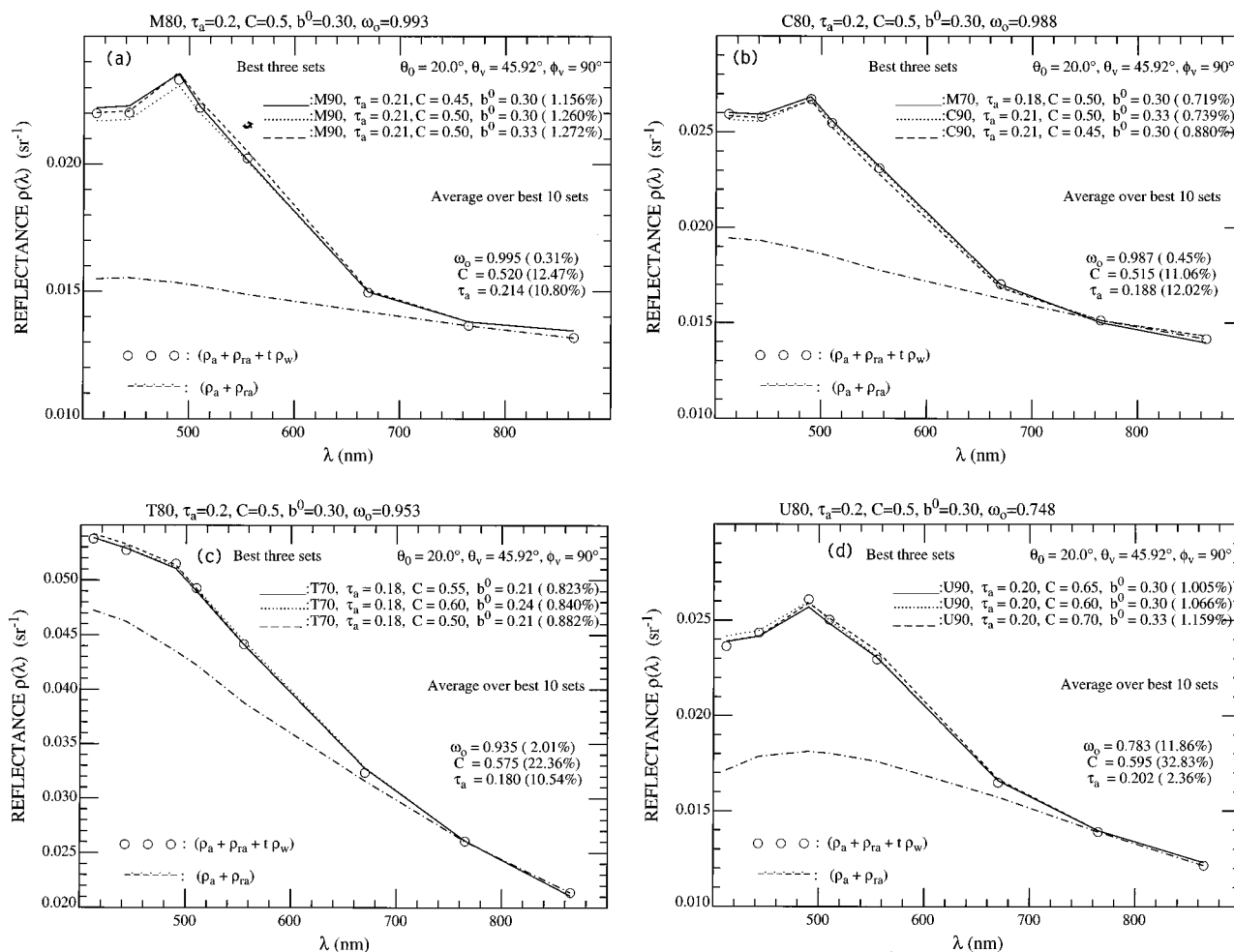

Fig. 3. Reflectance spectrum matching for pigment concentration $C = 0.50$ mg/m³ with Sun-viewing geometry of $\theta_0 = 20.0°$, $\theta_v = 45.92°$, and $\phi_v = 90.0°$: (a) M80, (b) C80, (c) T80, and (d) U80.
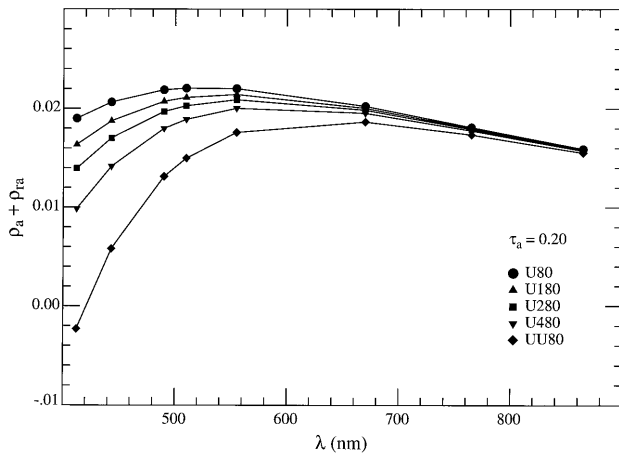
Fig. 4. Influence of the physical thickness of the aerosol layer on the spectrum of $\rho_a + \rho_{ra}$. For U80 the aerosol is confined to a thin layer near the surface, whereas for U180, U280, U480, and UU80, the aerosol is uniformly mixed with air to heights of 1, 2, and 4 km, and the whole atmosphere, respectively.

retrieval results for the pigment concentration C will still be good in the presence of small pigment concentration or small aerosol optical thickness. When both large aerosol optical thickness [$\tau_a(865)$ around 0.2–0.3] and large pigment concentration [C around 0.5–1.0 mg/m^3] are present in the atmosphere–ocean system, the performance of the algorithm is degraded. Still, for the worst case examined here, $\tau_a(865) = 0.3$ and $C = 1.0$ mg/m^3, ~60% of the individual simulations have $|\Delta C|/C < 30\%$. Note that when $\tau_a(865) = 0.3$, $\tau_a(443) = 0.347$, 0.395, 0.745, and 0.620 for M80, C80, T80, and U80, respectively, i.e., τ_a can be large in the blue, particularly for T80 and U80.

These simulations suggest that the success of the algorithm depends on the appropriateness of candidate aerosol models and the bio-optical model employed in the algorithm. Although we cannot determine the percent errors in the retrieved aerosol single-scattering albedo $\omega_0'(865)$ and pigment concentration C' by processing a satellite image, i.e., we do not know the correct answer, we can compute $\delta(A, \tau_a, C, b^0)'$ over all bands that are used for ocean color remote sensing. This provides one measure of the quality of the retrievals. Also, we can compute the percent deviations for retrieved $\omega_0'(865)$ and C' over the ten best models. Our results suggest that when the deviation in a retrieved quantity is small, its retrieval is more accurate.

4. Inclusion of the Aerosol Vertical Distribution

As mentioned in Section 1, when the aerosol is strongly absorbing, $\rho_a + \rho_{ra}$ depends significantly on the aerosol's vertical distribution (Fig. 4). In the simulations presented here, the correct vertical distribution was assumed, i.e., the pseudodata were created with the same vertical distribution as was assumed for the candidate aerosol models. It is reasonable to expect that the vertical distribution can be

introduced into the algorithm described in Section 2 simply as new candidate aerosol models, e.g., the U70 model with all the aerosol in the marine boundary layer and the U70 aerosol model with the aerosol uniformly mixed with air throughout the entire atmosphere would represent two distinct candidate aerosol models. This hypothesis is tested next.

As the vertical distribution of the aerosol is important only if it is strongly absorbing, we will consider vertical structure only in the urban models. In addition to the candidate urban models considered in Section 3, where the aerosol was all in the lower layer of a two-layer atmosphere with all the Rayleigh scattering confined to the upper layer, we now introduce three new vertical distributions: (1) the aerosol is uniformly mixed with air from the surface to an altitude of 2 km (21% of τ_r in the lower layer); (2) the aerosol is uniformly mixed with air from the surface to an altitude of 4 km (39% of τ_r in the lower layer); and (3) the aerosol is uniformly mixed with air throughout the entire atmosphere (all τ_r accompanies the aerosol in a one-layer atmosphere). These distributions for aerosol optical models U50, U70, U90, and U99 constitute 12 candidate aerosol models in addition to the 16 candidates in Section 3. Thus, for the algorithm tests described below, there are a grand total of 28 candidate aerosol models.

To test the algorithm's ability to deal with aerosol vertical structure, we created pseudodata with the U80 aerosol optical model with vertical structures similar to the candidate aerosol models, i.e., the aerosol mixed uniformly with air to an altitude of 2 km (U280), 4 km (U480), and uniformly mixed with air throughout the atmosphere (UU80). Figure 4 provides an example of the strong dependence of $\rho_a + \rho_{ra}$ on the vertical distribution of the aerosol for $\tau_a(865) = 0.2$ and the urban aerosol models with 80% RH. It is important to note from Fig. 4 that an uncertainty of ± 1 km in the thickness of the aerosol layer results in an uncertainty of $\sim \mp 0.002$ in $\rho_a + \rho_{ra}$ at 443 nm, i.e., equal in magnitude to the maximum acceptable uncertainty in ρ_w. Also, measurement of $\rho_a + \rho_{ra}$ in the NIR provides virtually no indication of the aerosol vertical structure even when the physical–chemical properties of the aerosol are known. As in the earlier sections, seven Sun-viewing geometries were investigated. The results of these tests can be summarized as follows:

1. The algorithm had no difficulty in concluding that the aerosol was strongly absorbing; however, the range in the retrieved ω_0 was from 0.606 to 0.821 (i.e., pure U70 to pure U90) over seven geometries, three vertical structures, and three values of $\tau_a(865)$, compared with the range 0.699–0.793 for U80 from Table 2. Thus, when vertical structure was included in the candidate aerosol models as described here, the actual value of ω_0 was not as accurate. The additional parameter (vertical distribution) provides an extra degree of freedom that allows ω_0 to take on a wider range of values and still provide a small δ'.

Table 7. Mean Values of Retrieved C for Seven Sun-Viewing Geometries and Three Aerosol Models (UU80, U280, U480)[a]

C (mg/m^3)	0.100	0.500	1.000
$\tau_a(865) = 0.100$	0.103 (8.74%)	0.600 (29.11%)	1.054 (19.27%)
$\tau_a(865) = 0.200$	0.114 (17.51%)	0.574 (39.12%)	1.026 (35.13%)
$\tau_a(865) = 0.300$	0.125 (32.93%)	0.644 (57.33%)	0.863 (52.53%)

[a]The standard deviation divided by the mean is listed in parentheses.

Table 10. Mean Values of Retrieved C for Seven Sun-Viewing Geometries of Aerosol Model U180[a]

C (mg/m^3)	0.100	0.500	1.000
$\tau_a(865) = 0.100$	0.100 (0.00%)	0.556 (7.15%)	1.094 (8.53%)
$\tau_a(865) = 0.200$	0.100 (0.00%)	0.544 (8.74%)	1.101 (16.12%)
$\tau_a(865) = 0.300$	0.100 (0.00%)	0.566 (3.04%)	1.061 (15.11%)

[a]The standard deviation divided by the mean is listed in parentheses.

2. For $C = 0.1$ and 0.5 mg/m^3, the aerosol models that were chosen as the ten best were nearly always all from the set with vertical structure; i.e., the candidates with the aerosol all at the bottom of the two-layer atmosphere were rarely chosen. The weakly absorbing aerosol models were never among the best ten.

3. For $C = 1$ mg/m^3, many of the UU80 retrievals were very poor; e.g., the retrieved C' was ~0.15 mg/m^3. In these cases, the UU70 candidate, which has too much absorption, was always chosen, requiring a smaller C to provide the additional reflectance needed in the blue. Similarly, for lower C, the UU80 cases tended to provide poorer results than the others; however, in all these cases with poor retrievals, δ' tended to be ~5–10 times larger than typical. These poor retrievals did not occur with the U280 and U480 cases, and probably could be avoided by using candidate models with a finer grid in ω_0 (Table 1).

4. The mean values of the retrieved C over seven geometries and three vertical distributions are shown in Table 7. The means are quite good (largest error ~30%), but the deviations are larger than those in Table 3. However, note that Table 7 includes the sometimes poor results for UU80 described in comment 3.

5. The distribution of $\Delta C/C$, as provided in Table 8, indicates that the error compares favorably with

the corresponding error in Table 5. The fraction of retrievals with $|\Delta C/C|$ less than a specified amount is smaller when vertical structure is included; however, unlike Table 5, which also includes weakly absorbing aerosols in the statistics, these statistics include only strongly absorbing aerosols.

6. The retrieved mean values of $\tau_a(865)$ show a small (~+5%) bias; however, the dispersion of $\tau_a(865)$ over seven geometries and three vertical structures is slightly less than those in Table 6.

These results all pertain to a situation in which the aerosol vertical structure was identical to that for some of the candidate models, although the aerosol optical model (size distribution and refractive index) was not among the candidate set. For completeness, we provide an additional example in which the pseudodata were created with the U80 aerosol optical model with the aerosol uniformly mixed to an altitude of 1 km. Thus, for this case, which we refer to as U180, neither the aerosol vertical structure nor the aerosol optical model are represented within the 28-member candidate aerosol set. The results of these simulations are provided in Tables 9–12 and show that the algorithm performs well in this particular situation.

The two tests presented in this section suggest that vertical structure for absorbing aerosols can be handled by including candidate vertical distributions within the candidate aerosol model set. In fact, considering that the results presented are for only strongly absorbing aerosols, the performance of the algorithm is excellent.

5. Effects of Error in $\rho_t - \rho_r - t\rho_{wc}$

In the absence of Sun glint, there are two important errors that can influence the performance of the algorithm: (1) error in $\rho_t(\lambda)$ resulting from the sensor's radiometric calibration error and (2) error in $\rho_{wc}(\lambda)$ resulting from natural noise[43] in the relationship between ρ_{wc} and the wind speed. Here we examine the effects of these errors.

Table 8. Percentage of Retrieved Pigment Concentration C Within Certain Error Limits for Aerosol Models UU80, U280, and U480

C (mg/m^3)	$\Delta C/C$	<5%	<10%	<20%	<30%
0.1	$\tau_a(865) = 0.100$	85%	85%	95%	95%
	$\tau_a(865) = 0.200$	57%	57%	71%	80%
	$\tau_a(865) = 0.300$	57%	57%	61%	61%
0.5	$\tau_a(865) = 0.100$	28%	52%	71%	90%
	$\tau_a(865) = 0.200$	38%	57%	66%	66%
	$\tau_a(865) = 0.300$	23%	38%	66%	66%
1.0	$\tau_a(865) = 0.100$	47%	66%	71%	76%
	$\tau_a(865) = 0.200$	19%	38%	52%	61%
	$\tau_a(865) = 0.300$	4%	28%	52%	57%

Table 9. Mean Values of Retrieved $\omega_0(865)$ for Seven Sun-Viewing Geometries of Aerosol Model U180[a]

	C (mg/m^3)	0.100	0.500	1.000
U180	$\tau_a(865) = 0.100$	0.764 (4.81%)	0.787 (6.82%)	0.787 (4.88%)
$\omega_0 = 0.748$	$\tau_a(865) = 0.200$	0.737 (3.24%)	0.737 (8.84%)	0.723 (13.50%)
	$\tau_a(865) = 0.300$	0.736 (4.31%)	0.727 (4.39%)	0.714 (8.86%)

[a]The standard deviation divided by the mean is listed in parentheses.

Table 11. Percentage of Retrieved Pigment Concentration C Within Certain Error Limits for the Aerosol Model U180

C (mg/m^3)	$\Delta C/C$	<5%	<10%	<20%	<30%
0.1	$\tau_a(865) = 0.100$	100%	100%	100%	100%
	$\tau_a(865) = 0.200$	100%	100%	100%	100%
	$\tau_a(865) = 0.300$	100%	100%	100%	100%
0.5	$\tau_a(865) = 0.100$	28%	42%	71%	100%
	$\tau_a(865) = 0.200$	14%	42%	100%	100%
	$\tau_a(865) = 0.300$	0%	14%	100%	100%
1.0	$\tau_a(865) = 0.100$	28%	57%	85%	100%
	$\tau_a(865) = 0.200$	0%	28%	57%	100%
	$\tau_a(865) = 0.300$	28%	28%	71%	100%

Table 13. Values of the Residual Radiometric Calibration Uncertainty After Affecting an In-orbit Calibration Adjustment[45]

λ_i (nm)	Uncertainty (%)
412	0.3
443	0.5
490	0.8
520	1.0
550	1.5
670	2.0
765	3.0
865	5.0

A. Error in $\rho_t(\lambda)$

There will always be some error in the radiometric calibration of the sensor. The specifications for MODIS and SeaWIFS require that the uncertainty in the prelaunch calibration be less than 5% and 10%, respectively. As the goal is to recover the water-leaving radiance (reflectance) with an error of $\lesssim \pm 5\%$ at 443 nm in clear ocean water, e.g., the Sargasso Sea in summer, where under such conditions the water-leaving radiance is expected to contribute $\sim 10\%$ to $L_t(443)$, a 5–10% error in L_t is clearly unacceptable. Thus, in-orbit calibration adjustments are required.[44] Evans and Gordon[10] described methodology used to perform such adjustments for CZCS, and Gordon[12] sketched a possible procedure for SeaWIFS and MODIS. In principle, Gordon's SeaWIFS/MODIS procedure should be capable of reducing the calibration uncertainty in the blue to 0.5%. In fact, by simultaneously measuring $\rho_w(\lambda)$, $\rho_{wc}(\lambda)$, and $\tau_a(\lambda)$, Gordon[45] argued that for MODIS with a prelaunch calibration uncertainty of $\pm 5\%$, it should be possible in principle to reduce the calibration errors of the other bands to those shown in Table 13 and to ensure that the residual calibration errors all have the same sign as the error at 865 nm. This is possible because of the known, and rapidly increasing with decreasing wavelength, contribution of ρ_r to ρ_t. Here we assume that this procedure has been affected and that the sensor has the calibration errors of magnitude shown in Table 13.

We added positive and negative calibration errors to the ρ_t pseudodata described in Section 3 for the M80, C80, T80, and U80 aerosol models and operated the algorithm. Generally, there were no large changes in the results. As before, the algorithm had no difficulty distinguishing between strongly and weakly absorbing aerosols. The statistics of the distribution in $\Delta C/C$ were similar to those in Table 5. The derived τ_a followed the expected trend, i.e., positive error led to greater values of τ_a. As an example of the retrieved pigment concentration statistics, Table 14 provides the mean C and its standard deviation over the 28 cases in the absence and presence of calibration errors. We see that the effect of the calibration error is to increase the dispersion with only minor changes in the mean values. This insensitivity to residual calibration errors results from the fact that they are small in the blue (Table 13).

B. Error in $\rho_{wc}(\lambda)$

The whitecap reflectance contribution $t\rho_{wc}$ can be estimated given the wind speed.[43,46] Gordon and Wang[43] show that $t\rho_{wc}$ is given by

$$t(\lambda)\rho_{wc}(\lambda) = [\rho_{wc}(\lambda)]_N t(\theta_0, \lambda) t(\theta_v, \lambda),$$

where $[\rho_{wc}(\lambda)]_N$ is the average increase in the reflectance of the ocean (over several pixels) at the sea surface, resulting from whitecaps in the absence of the atmosphere. It can be thought of as the product of the albedo of an individual whitecap and the fraction of the sea surface covered by whitecaps. $t(\theta_v, \lambda)$ is given in Eq. (3) and $t(\theta_0, \lambda)$ is also given by Eq. (3) with θ_v replaced by θ_0. In the visible, for a wind speed of 10 m/s $[\rho_{wc}(\lambda)]_N$ varies from ~ 0 to 0.004 with a mean of ~ 0.002.[43] Thus, given a wind speed of 10 m/s, the prediction of $[\rho_{wc}(\lambda)]_N$ would be 0.002 $\pm$ 0.002 in the visible. The spectrum of $[\rho_{wc}(\lambda)]_N$ was originally taken to be white[43]; however, measurements by Frouin *et al.*[47] in the surf zone suggest that the reflectance may decrease considerably in passing

Table 12. Mean Values of Retrieved $\tau_a(865)$ for Seven Sun-Viewing Geometries of the Aerosol Model U180[a]

C (mg/m^3)	0.100	0.500	1.000
$\tau_a(865) = 0.100$	0.102 (1.68%)	0.101 (3.62%)	0.099 (3.83%)
$\tau_a(865) = 0.200$	0.206 (3.49%)	0.206 (2.89%)	0.209 (7.59%)
$\tau_a(865) = 0.300$	0.305 (3.32%)	0.307 (2.52%)	0.304 (7.36%)

[a]The standard deviation divided by the mean is listed in parentheses.

Table 14. Mean Values of the Retrieved C for the Seven Sun-Viewing Geometries and Each of Four Aerosol Models (M80, C80, T80, U80) for the Indicated Calibration Error (Table 13)[a]

Calibration Error	C (mg/m^3)		
	0.100	0.500	1.000
Positive Error	0.102 (4.3%)	0.539 (15.1%)	0.976 (21.2%)
Zero Error	0.100 (3.1%)	0.470 (4.7%)	0.940 (12.8%)
Negative Error	0.100 (5.7%)	0.534 (15.9%)	1.029 (23.3%)

[a]The standard deviation divided by the mean is listed in parentheses. $\tau_a(865) = 0.2$.

Table 15. Mean Values of Retrieved C for Seven Sun-Viewing Geometries and Four Aerosol Models (M80, C80, T80, U80) for $\Delta[\rho_{wc}] = +0.002^a$

C (mg/m^3)	0.100	0.500	1.000
$\tau_a(865) = 0.100$	0.100 (0.00%)	0.455 (9.54%)	0.838 (19.89%)
$\tau_a(865) = 0.200$	0.101 (4.68%)	0.485 (15.72%)	0.891 (23.44%)
$\tau_a(865) = 0.300$	0.102 (6.97%)	0.526 (18.80%)	0.843 (25.55%)

^{a}The standard deviation divided by the mean is listed in parentheses.

from the visible to the NIR. By using the Frouin *et al.*[47] whitecap spectrum, we investigated the behavior of the algorithm for the M80, C80, T80, and U80 test models, given a ±0.002 error in $[\rho_{wc}(\lambda)]_N$ in the visible when removing $t\rho_{wc}$ from ρ_t. The simulations showed that the presence of a strongly absorbing aerosol could still be established with ease; however, ω_0 was larger (smaller) for a positive (negative) error in $t\rho_{wc}$. The variation in ω_0 was ~±5% for the U80 test. Conversely, τ_a was smaller (larger) for a positive (negative) error in $t\rho_{wc}$. The magnitude of the changes in τ_a was ~10–15% for all the test models. The variation in τ_a is easy to understand. If $[\rho_{wc}]_N$ is overestimated, $\rho_a + \rho_{ra}$ will be too small, leading to a value of τ_a that is too small.

The average values of C' were not strongly influenced by the error in $[\rho_{wc}]_N$. This can be seen in Tables 15 and 16 for error in $[\rho_{wc}]_N$, $\Delta[\rho_{wc}]_N$, in the visible of +0.002 and −0.002, respectively. These should be compared with Table 3 for $\Delta[\rho_{wc}]_N = 0$. The whitecap error causes a variation of ±10–15% in C' at the higher pigment concentrations but has little effect at $C = 0.1$ mg/m^3. The distributions of $|\Delta C|/C$ less than a given fraction actually improve for $\Delta[\rho_{wc}]_N = +0.002$, e.g., for $C = 1$ mg/m^3 and $\tau_a = 0.3$, the fraction with $|\Delta C|/C < 30\%$ was 53, 60, and 82% for $\Delta[\rho_{wc}]_N = -0.002$, 0, and +0.002, respectively.

Examination of the individual retrievals shows that in the case of the strongly absorbing aerosols, the bias introduced by the whitecap error causes the same incorrect aerosol model to be always chosen among the best ten; e.g., either U70 or U90 was always chosen when the correct model was U80. This biases the individual retrievals of C, ω_0, and τ_a to always be too high or too low, and thus the averages are as well. This effect may be reduced by increased resolution in the model values of ω_0. Similar effects were observed in the case of sensor calibration errors (Subsection 5.A). These simulations suggest that

Table 16. Mean Values of Retrieved C for Seven Sun-Viewing Geometries and Four Aerosol Models (M80, C80, T80, U80) for $\Delta[\rho_{wc}] = -0.002^a$

C (mg/m^3)	0.100	0.500	1.000
$\tau_a(865) = 0.100$	0.100 (0.94%)	0.647 (12.83%)	1.175 (18.21%)
$\tau_a(865) = 0.200$	0.100 (2.32%)	0.644 (17.53%)	1.030 (24.13%)
$\tau_a(865) = 0.300$	0.101 (4.96%)	0.699 (24.94%)	0.985 (31.03%)

^{a}The standard deviation divided by the mean is listed in parentheses.

the algorithm is not overly sensitive to error in removing the whitecap reflectance component from ρ_t.

6. Discussion

Current atmospheric correction algorithms for ocean color sensors operating over case 1 waters use measurements of the TOA reflectance in the NIR, where the contribution for the ocean is known, to assess the aerosol optical properties. Such measurements are incapable of distinguishing between weakly and strongly absorbing aerosols, and atmospheric correction fails if the incorrect absorption properties of the aerosol are assumed.[12] Similarly, algorithms for extracting aerosol properties from passive spaceborne sensors operating in the red and NIR are also incapable of detecting absorption[48] because the aerosol component of the TOA reflectance is proportional to the scattering optical thickness ($\omega_0\tau_a$); i.e., ω_0 cannot be separated from τ_a. However, it has been shown that it is possible to retrieve spatial distributions of an index indicating the presence of strongly absorbing aerosols by using the Total Ozone Mapping Spectrometer measurements in the ultraviolet,[25] where there is significant multiple scattering even in the absence of aerosols. The effect of aerosol absorption on the TOA reflectance becomes stronger as multiple scattering increases. This suggested to us that it would be possible to determine aerosol absorption with ocean color sensors only by utilizing observations in the blue, where, unfortunately, the contribution to the TOA reflectance by the aerosol and by the radiance exiting the ocean are comparable. Thus utilizing the blue portion of the spectrum requires simultaneous determination of the water-leaving reflectance and the aerosol's contribution to the TOA reflectance.

In this paper we have presented an algorithm that appears promising for the retrieval of in-water biophysical properties and aerosol optical properties in atmospheres containing both weakly and strongly absorbing aerosols. By using the entire spectrum available to most ocean color instruments (412–865 nm), we simultaneously recover the ocean's bio-optical properties and a set of aerosol models that best describe the aerosol optical properties. As an example, the algorithm has been applied to situations that are likely to occur off the U.S. East Coast in summer when the aerosols could be of the locally generated weakly absorbing Maritime type or of the pollution-generated strongly absorbing urban-type transported over the ocean by the winds. Through simulations, we show that the algorithm behaves as well in an atmosphere with weakly or strongly absorbing aerosol as the Gordon and Wang[11] algorithm does in an atmosphere with only weakly absorbing aerosols. In contrast to earlier algorithms,[26–28] the present algorithm successfully identifies absorbing aerosols and provides close values for their optical thickness.

The algorithm requires a bio-optical model of the ocean[30] and a set of aerosol models for its operation. The parameters of the bio-optical model and the aero-

sol models are systematically varied to find the best (in an rms sense) fit to the measured TOA spectral reflectance. It is critical that the aerosol models be representative of the aerosol expected to be present over the given area, e.g., the urban models used here would not be expected to yield useful retrievals in a region subjected to absorbing mineral dust.[14] Also, it is necessary that aerosol models encompass the range of aerosol vertical distributions expected. As adequate bio-optical models are available only for case 1 waters,[5,26,30,49,50] the current algorithm would not operate successfully in case 2 waters; however, given region specific models for case 2 waters, comparable performance may be possible as long as the spectral variation of ρ_w and $\rho_a + \rho_{ra}$ are sufficiently different.[28] Fortunately, case 1 waters include most of the open ocean.

A general observation from examining the individual retrievals (both weakly and strongly absorbing and vertically distributed) is that for low C the algorithm will generally choose a value of C that is close to the correct value with little dispersion over the ten best sets. This is owing to the fact that the $\rho_w(\lambda)$ is a strong function of C and λ for small C (Fig. 1), and this provides a strong constraint on the range of values possible. Thus, by using the nearly correct C, the algorithm apparently varies the aerosol model and τ_a seeking the optimum set. This results in a larger dispersion in τ_a and ω_0 than in C. In contrast, for large C, where $\rho_w(\lambda)$ depends weakly on both C and λ (Fig. 1) and is small itself, the aerosol model typically provides the stronger constraint, and ω_0 along with τ_a are retrieved with small dispersions, whereas the algorithm optimizes δ' by varying C and b^0. This causes a larger dispersion in C'. Generally, we find that the quantities with low dispersion over the ten best sets are retrieved more accurately than quantities with a large dispersion.

We intend to utilize this algorithm for processing SeaWIFS and MODIS imagery. In its present research implementation the algorithm is slow because a brute-force determination of the best ten sets of parameters is employed. However, alternative formulations are faster. For example, as we know $\rho_w(865) = 0$, $\rho_a(865) + \rho_{ra}(865)$ can be retrieved unambiguously from the imagery. For a given aerosol model the value of $\tau_a(865)$ that yields the retrieved $\rho_a(865) + \rho_{ra}(865)$ can be found directly. Thus, for each model these is really no reason to vary $\tau_a(865)$. When 16 aerosol models are used, this reduces the number of elements in the testing set from 230,000 to 5760. The resulting solution will not be identical to the method based on minimizing δ' in Eq. (6), because now for each set the residual error at 865 nm will be exactly zero; i.e., in Fig. 3 every set would exactly pass through the point at $\lambda = 865$ nm. We have used this method to examine the test cases in Section 3, and, as expected, the results are not identical to those presented earlier (Tables 2, 3, 5, and 6), but there are no significant differences. To further reduce the number of test sets, we used the Gordon and Wang[11] algorithm to preselect models. Based on their spec-

tral variation in the NIR, the Gordon and Wang algorithm operationally selects the best four models from the set of candidates. Employing this for the tests in Section 3 reduced the number of test sets by an additional factor of 4 to 1440. Again, there were no significant differences compared with the earlier results. We note, however, that as vertical structure is irrelevant to the spectral behavior in the NIR (Fig. 4), if strongly absorbing models are chosen by the Gordon and Wang algorithm, models with the same optical characteristics but different vertical structures should be included in the test set. For the examples in Section 4 there were a total of 28 models used as candidates, leading to 403,200 test sets; with the two improvements above, this would be reduced to 3600 assuming that the Gordon and Wang algorithm would choose two strongly absorbing and two weakly absorbing aerosol models. This is the approach we intend to use for SeaWIFS and MODIS.

In reality, we see no need to apply the new algorithm on a pixel-by-pixel basis. We believe a viable strategy would be to employ it at the center of $N \times N$ pixel regions, where $N \sim 10$–100, to determine the best aerosol models, and then use the faster Gordon and Wang[11] algorithm, with a restricted set of models that are determined by the new algorithm. This strategy assumes that the only property of the aerosol that changes within the $N \times N$ region is the aerosol concentration.

A possible method for improving the algorithm is to use the linear-mixing model of Wang and Gordon,[51] as improved by Abdou *et al.*,[52] and to vary the mixing ratios of a fixed set of aerosol components, rather than using a fixed set of aerosol models. This is similar in spirit to the Land and Haigh[28] approach. Wang and Gordon[39] have shown that such a method holds promise for estimating the size distribution of weakly absorbing aerosols with simulated Multiangle Imaging Spectroradiometer[53] data.

References

1. W. A. Hovis, D. K. Clark, F. Anderson, R. W. Austin, W. H. Wilson, E. T. Baker, D. Ball, H. R. Gordon, J. L. Mueller, S. Y. E. Sayed, B. Strum, R. C. Wrigley, and C. S. Yentsch, "Nimbus 7 coastal zone color scanner: system description and initial imagery," Science **210**, 60–63 (1980).
2. H. R. Gordon, D. K. Clark, J. L. Mueller, and W. A. Hovis, "Phytoplankton pigments derived from the Nimbus-7 CZCS: initial comparisons with surface measurements," Science **210,** 63–66 (1980).
3. S. B. Hooker, W. E. Esaias, G. C. Feldman, W. W. Gregg, and C. R. McClain, "SeaWiFS Technical Report Series: Volume 1, An Overview of SeaWiFS and Ocean Color," NASA Tech. Mem. 104566 (NASA, Greenbelt, Md., 1992).
4. V. V. Salomonson, W. L. Barnes, P. W. Maymon, H. E. Montgomery, and H. Ostrow, "MODIS: advanced facility instrument for studies of the Earth as a system," IEEE Geosci. Remote Sens. **27,** 145–152 (1989).
5. H. R. Gordon and A. Y. Morel, *Remote Assessment of Ocean*

Color for Interpretation of Satellite Visible Imagery: a Review (Springer-Verlag, New York, 1983).

6. H. R. Gordon, D. K. Clark, J. W. Brown, O. B. Brown, R. H. Evans, and W. W. Broenkow, "Phytoplankton pigment concentrations in the Middle Atlantic Bight: comparison between ship determinations and Coastal Zone Color Scanner estimates," Appl. Opt. **22,** 20–36 (1983).

7. H. R. Gordon, "Removal of atmospheric effects from satellite imagery of the oceans," Appl. Opt. **17,** 1631–1636 (1978).

8. H. R. Gordon and D. K. Clark, "Atmospheric effects in the remote sensing of phytoplankton pigments," Boundary Layer Meteorol. **18,** 299–313 (1980).

9. H. R. Gordon, J. W. Brown, and R. H. Evans, "Exact Rayleigh scattering calculations for use with the Nimbus-7 Coastal Zone Color Scanner," Appl. Opt. **27,** 862–871 (1988).

10. R. H. Evans and H. R. Gordon, "CZCS 'system calibration:' a retrospective examination," J. Geophys. Res. **99,** 7293–7307 (1994).

11. H. R. Gordon and M. Wang, "Retrieval of water-leaving radiance and aerosol optical thickness over the oceans with Sea-WIFS: a preliminary algorithm," Appl. Opt. **33,** 443–452 (1994).

12. H. R. Gordon, "Atmospheric correction of ocean color imagery in the Earth Observing System era," J. Geophys. Res. **102D,** 17,081–17,106 (1997).

13. G. A. d'Almeida, P. Koepke, and E. P. Shettle, *Atmospheric Aerosols—Global Climatology and Radiative Characteristics* (Deepak, Hampton, Va., 1991).

14. T. Nakajima, M. Tanaka, M. Yamano, M. Shiobara, K. Arao, and Y. Nakanishi, "Aerosol optical characteristics in the yellow sand events observed in May 1982 at Nagasaki—Part II: models," J. Meteorol. Soc. Jpn. **67,** 279–291 (1989).

15. R. W. Young, K. L. Carder, P. R. Betzer, D. K. Costello, R. A. Duce, G. R. Ditullio, N. W. Tindale, E. A. Laws, M. Uematsu, J. T. Merrill, and R. A. Feeley, "Atmospheric iron inputs and primary productivity: phytoplankton responses in the North Pacific," Global Biogeochem. Cycles **5,** 119–134 (1991).

16. R. J. Charlson, S. E. Schwartz, J. M. Hales, R. D. Cess, J. A. Coakley, J. E. Hansen, and D. J. Hofmann, "Climate forcing by anthropogenic aerosols," Science **255,** 423–430 (1992).

17. Y. J. Kaufman, "Remote sensing of direct and indirect aerosol forcing," in *Aerosol Forcing of Climate*, R. H. Charlson and J. Heintzenberg, eds. (Wiley, New York, 1995), pp. 297–332.

18. M. Griggs, "Measurements of the aerosol optical thickness over water using ERTS-1 data," J. Air Pollut. Control. Assoc. **25,** 622–626 (1975).

19. Y. Mekler, H. Quenzel, G. Ohring, and I. Marcus, "Relative atmospheric aerosol content from Erts observations," J. Geophys. Res. **82,** 967–970 (1977).

20. R. S. Fraser, "Satellite measurement of mass of Sahara dust in the atmosphere," Appl. Opt. **15,** 2471–2479 (1976).

21. P. Koepke and H. Quenzel, "Turbidity of the atmosphere determined from satellite: calculation of optimum viewing geometry," J. Geophys. Res. **84,** 7847–7856 (1979).

22. P. Koepke and H. Quenzel, "Turbidity of the atmosphere determined from satellite: calculation of optimum wavelength," J. Geophys. Res. **86,** 9801–9805 (1981).

23. P. A. Durkee, D. R. Jensen, E. E. Hindman, and T. H. V. Haar, "The relationship between marine aerosol particles and satellite-detected radiance," J. Geophys. Res. **91,** 4063–4072 (1986).

24. C. R. N. Rao, L. L. Stowe, E. P. McClain, and J. Sapper, "Development and application of aerosol remote sensing with AVHRR data from the NOAA satellites," in *Aerosols and Climate*, P. Hobbs and M. P. McCormick, eds. (Deepak, Hampton, Va., 1988), pp. 69–80.

25. J. R. Herman, P. K. Bhartia, O. Torres, C. Hsu, and C. Seftor, "Global distribution of UV-absorbing aerosols from Nimbus 7/TOMS data," J. Geophys. Res. **102D,** 16,911–16,922 (1997).

26. A. Bricaud and A. Morel, "Atmospheric corrections and interpretation of marine radiances in CZCS imagery: use of a reflectance model," Oceanolog. Acta **7,** 33–50 (1987).

27. J.-M. André and A. Morel, "Atmospheric corrections and interpretation of marine radiances in CZCS imagery, revisited," Oceanolog. Acta **14,** 3–22 (1991).

28. P. E. Land and J. D. Haigh, "Atmospheric correction over case 2 waters with an iterative fitting algorithm," Appl. Opt. **35,** 5443–5451 (1996).

29. J. E. Hansen and L. D. Travis, "Light scattering in planetary atmospheres," Space Sci. Rev. **16,** 527–610 (1974).

30. H. R. Gordon, O. B. Brown, R. H. Evans, J. W. Brown, R. C. Smith, K. S. Baker, and D. K. Clark, "A semi-analytic radiance model of ocean color," J. Geophys. Res. **93,** 10,909–10,924 (1988).

31. A. Morel and L. Prieur, "Analysis of variations in ocean color," Limnol. Oceanogr. **22,** 709–722 (1977).

32. A. Morel and B. Gentili, "Diffuse reflectance of oceanic waters: its dependence on Sun angle as influenced by the molecular scattering contribution," Appl. Opt. **30,** 4427–4438 (1991).

33. A. Morel and B. Gentili, "Diffuse reflectance of oceanic waters. II. bidirectional aspects," Appl. Opt. **32,** 6864–6879 (1993).

34. A. Morel, K. J. Voss, and B. Gentili, "Bidirectional reflectance of oceanic waters: a comparison of modeled and measured upward radiance fields," J. Geophys. Res. **100,** 13,143–13,150 (1995).

35. A. Morel and B. Gentili, "Diffuse reflectance of oceanic waters. III. Implication of bidirectionality for the remote sensing problem," Appl. Opt. **35,** 4850–4862 (1996).

36. D. Tanre, M. Herman, P. Y. Deschamps, and A. de Leffe, "Atmospheric modeling for space measurements of ground reflectances, including bidirectional properties," Appl. Opt. **18,** 3587–3594 (1979).

37. H. Yang and H. R. Gordon, "Remote sensing of ocean color: assessment of the water-leaving radiance bidirectional effects on the atmospheric diffuse transmittance," Appl. Opt. **36,** 7887–7897 (1997).

38. M. Wang and H. R. Gordon, "Estimating aerosol optical properties over the oceans with the multiangle imaging spectroradiometer: some preliminary studies," Appl. Opt. **33,** 4042–4057 (1994).

39. M. Wang and H. R. Gordon, "Estimation of aerosol columnar size distribution and optical thickness from the angular distribution of radiance exiting the atmosphere: simulations," Appl. Opt. **34,** 6989–7001 (1995).

40. E. P. Shettle and R. W. Fenn, "Models for the aerosols of the lower atmosphere and the effects of humidity variations on their optical properties," Tech. Rep. AFGL-TR-79-0214, 1979 (Air Force Geophysics Laboratory, Hanscomb Air Force Base, Mass.).

41. F. X. Kenizys, E. P. Shettle, W. O. Gallery, J. H. Chetwynd, L. W. Abreu, J. E. A. Selby, S. A. Clough, and R. W. Fenn, "Atmospheric transmittance/radiance: the LOWTRAN 6 model," Tech. Rep. AFGL-TR-83-0187, 1983 (Air Force Geophysics Laboratory, Hanscomb Air Force Base, Mass.)

42. W. H. Press, B. P. Flannery, S. A. Teukolsky, and W. T. Vetterling, *Numerical Recipes in FORTRAN* (Cambridge U. Press, Cambridge, England, 1992).

43. H. R. Gordon and M. Wang, "Influence of oceanic whitecaps on atmospheric correction of SeaWIFS," Appl. Opt. **33,** 7754–7763 (1994).

44. H. R. Gordon, "Calibration requirements and methodology for remote sensors viewing the oceans in the visible," Remote Sensing Environ. **22,** 103–126 (1987).

45. H. R. Gordon, "In-orbit calibration strategy for vicarious cali-

bration of ocean color sensors," Remote Sens. Environ. (to be published).

46. P. Koepke, "Effective reflectance of oceanic whitecaps," Appl. Opt. **23,** 1816–1824 (1984).

47. R. Frouin, M. Schwindling, and P. Y. Deschamps, "Spectral reflectance of sea foam in the visible and near-infrared: in-situ measurements and implications for remote sensing of ocean color and aerosols," J. Geophys. Res. **101,** 14,361–14,371 (1996).

48. R. B. Husar, L. L. Stowe, and J. M. Prospero, "Satellite sensing of tropospheric aerosols over the oceans with NOAA AVHRR," J. Geophys. Res. **102D,** 16,889–16,909 (1997).

49. A. Morel, "Optical modeling of the upper ocean in relation to its biogenous matter content (case I waters)," J. Geophys. Res. **93,** 10,749–10,768 (1988).

50. Z. P. Lee, K. L. Carder, S. K. Hawes, R. G. Steward, T. G. Peacock, and C. O. Davis, "Method to derive ocean absorption coefficients from remote sensing reflectance," Appl. Opt. **35,** 453–462 (1996).

51. M. Wang and H. R. Gordon, "Radiance reflected from the ocean-atmosphere system: synthesis from individual components of the aerosol size distribution," Appl. Opt. **33,** 7088–7095 (1994).

52. W. A. Abdou, J. V. Martonchik, R. A. Kahn, R. A. West, and D. J. Diner, "A modified linear-mixing method for calculating atmospheric path radiances of aerosol mixtures," J. Geophys. Res. **102D,** 16,883–16,888 (1997).

53. D. J. Diner, C. J. Bruegge, J. V. Martonchik, T. P. Ackerman, R. Davies, S. A. W. Gerstl, H. R. Gordon, P. J. Sellers, J. Clark, J. A. Daniels, E. D. Danielson, V. G. Duval, K. P. Klaasen, G. W. L. A. D. I. Nakamoto, R. Pagano, and T. H. Reilly, "MISR: a multi-angle imaging spectroradiometer for geophysical and climatological research from EOS," IEEE Trans. Geosci. Remote Sensing **27,** 200–214 (1989).